DOI: 10.13009/EUCASS2019-1026

On modelling the finite strain anisotropic elastoplasticity with application to the prediction of springback in sheet metal forming

Raúl Díaz González[⋆]*, Miguel Ángel Sanz Gómez.*[⋆†] *and Khanh Nguyen Gia*[⋆]
[⋆]*E.T.S.I. Aeronáutica y Espacio*
Universidad Politécnica de Madrid, Plaza del Cardenal Cisneros, 3, 28040 Madrid
raul.diaz.gonzalez@alumnos.upm.es · miguelangel.sanz@upm.es · khanhnguyen.gia@upm.es

Abstract

In this paper we present a new computational framework for finite strain elastoplasticity applied to the springback analysis. The computational algorithm includes both elastic and plastic anisotropy and kinematic-isotropic hardening. The formulation solves the elastoplastic problem through a new corrector-predictor-type algorithm in the logarithmic strain space, with the novelty to present an elastic corrector instead of the classical plastic predictor. The springback analysis with finite element is important to predict the shape of sheet metal parts manufactured by plastic forming. The springback simulation has been performed with the commercial program ADINA® and a user subroutine implementing the computational algorithm.

1. Introduction

The springback phenomenon is a undesirable change in the final shape of metal forming manufactured parts, that occurs when the unloading follows the plastic forming process. This unavoidable effect has a great dependence on the elastoplastic material properties, specially on the plastic evolution and strain hardening of the metallic materials. The geometry is also another important aspect to take into account if large displacements are present and the overall geometry has large aspect ratios between the main dimensions.

The primary issue to successfully simulate the springback on an elastoplastic problem is related to the behaviour of the metallic materials and the constitutive model considered, where the plastic hardening is the responsible of the final deformations and residual stress resultant in the forming process. Sheet metals exhibit anisotropic plastic behaviour due to the macroscopic texture, a property dependent on the metallic grain morphology and distribution, and their oriented microstructure. During the forming process, when large deformations take place, anisotropy causes important effects over the final shape of the metallic parts, like an anisotropic distribution in the elastic strains and the appearance of sensitive residual stresses, or the earing in the deep drawing forming of cylindrical cups. In the aeronautic industry, one important problem due to this usually undesirable effect is the springback on the forming of wing leading edges or other sheet metal parts that require a large strain forming.

The main objective of this paper is showing the robustness and applicability of the novel framework [1] to simulate and predict a complex springback benchmark. To this end, in the next section we describe the formulation used in this paper, which is implemented as a user subroutine in the commercial finite element program ADINA®. After that, we demonstrate the applicability of the approach to prediction of springback phenomenon in sheet metal forming benchmarks and perform a comparison with established formulations.

2. Continuum theory and algorithmic framework in the elastoplastic model

In this section we show the most important aspects of the continuum theory and the algorithmic framework employed to the stress integration. For a further understanding of the framework used in this paper, the reading of [1, 2] is highly recommended.

The material model combined hardening is motivated from the rheological model shown in Fig. 1. This phenomenological macroscopic model may be described for infinitesimal strains in an appropriate interpretation, commonly referred as small strains, where $\boldsymbol{\varepsilon}$ and $\boldsymbol{\sigma}$ are the measurable variables, strain and tress respectively, and later

DOI: 10.13009/EUCASS2019-1026

permit us an easy extension to the respective variables $\boldsymbol{E}$ and $\boldsymbol{T}$ to define the elastoplastic behaviour in finite strains, commonly referred as large strains.

The device includes one dissipative Prandtl-type branch with a friction element in a series disposition with an elastic hookean spring, named as the internal branch. It is into this last branch where the internal state variables (elastic strain and plastic strain) operates simultaneously. The second branch is placed in a parallel arrangement with the internal branch, and contains an only spring Hooke-type element. This second branch is responsible for the macroscopic kinematic hardening, referred as the kinematic branch, and where only the external variable total strain operates. This approach avoids the use of additional internal variables in the continuum formulation kinematic hardening in the plastic evolution, like the backstress present in other classical models.

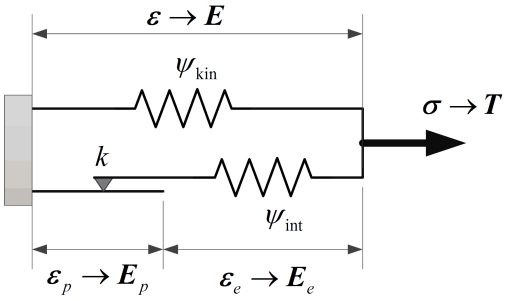

Figure 1: Rheological device motivating the anisotropic finite elastoplasticity model, with nonlinear combined isotropic and kinematic hardening.

The model employs a Lee-type multiplicative decomposition over the deformation gradient $\boldsymbol{F}$, split in an elastic part $\boldsymbol{F}_e$ and a plastic part $\boldsymbol{F}_p$ in order to obtain the internal state variables placed in the rheological model presented in Fig. 1.

$$\boldsymbol{F} = \boldsymbol{F}_e \boldsymbol{F}_p \tag{1}$$

At this point, we are interested in the use of a logarithmic strain framework. This strain measure offers an interesting additive quality, and Eq. 1 allows us to describe the logarithmic strain tensor variables in a natural form: $\boldsymbol{E}_e = \frac{1}{2}\ln(\boldsymbol{F}_e^T \boldsymbol{F}_e)$ and $\boldsymbol{E} = \frac{1}{2}\ln(\boldsymbol{F}^T \boldsymbol{F})$, in their respective configurations, and obtain the important internal state variable dependence $\boldsymbol{E}_e(\boldsymbol{E}, \boldsymbol{F}_p)$. This operation is of great importance int this work for the algorithmic elastoplastic problem, because it will permit us to decompose the strain rate tensor into the natural addition of two partial contributions in the incremental continuum theory

$$\dot{\boldsymbol{E}}_e(\dot{\boldsymbol{E}}, \dot{\boldsymbol{F}}_p) = \left.\frac{\partial \boldsymbol{E}_e}{\partial \boldsymbol{E}}\right|_{\dot{\boldsymbol{F}}_p = \boldsymbol{0}} : \dot{\boldsymbol{E}} + \left.\frac{\partial \boldsymbol{E}_e}{\partial \boldsymbol{F}_p}\right|_{\dot{\boldsymbol{E}} = \boldsymbol{0}} : \dot{\boldsymbol{F}}_p = \dot{\boldsymbol{E}}_e|_{\dot{\boldsymbol{F}}_p = \boldsymbol{0}} + \dot{\boldsymbol{E}}_e|_{\dot{\boldsymbol{E}} = \boldsymbol{0}} \tag{2}$$

where the first addend is obtained within a continuum framework, when the internal evolution variable (dissipative plastic strain rate) is frozen, whereas the second addend is obtained when the external evolution variable (total strain rate) is frozen. This last mentioned condition occurs when internal evolution is allowed in the incremental algorithmic framework, where these events occur incrementally and sequentially. This additive split operation is in fact, equivalent to the classical corrector-predictor scheme, and Eq. 2 may be read as

$$\dot{\boldsymbol{E}}_e(\dot{\boldsymbol{E}}, \dot{\boldsymbol{F}}_p) = \dot{\boldsymbol{E}}_e|_{\dot{\boldsymbol{F}}_p = \boldsymbol{0}} + \dot{\boldsymbol{E}}_e|_{\dot{\boldsymbol{E}} = \boldsymbol{0}} = {}^{tr}\dot{\boldsymbol{E}}_e + {}^{ct}\dot{\boldsymbol{E}}_e \tag{3}$$

where ${}^{tr}\dot{\boldsymbol{E}}_e$ is the predictor term, or trial elastic contribution to the elastic logarithmic strain rate tensor $\dot{\boldsymbol{E}}_e$ and depends on the logarithmic strain rate $\dot{\boldsymbol{E}}$ only, when the plastic evolution is frozen ($\dot{\boldsymbol{F}}_p = 0$) in the continuum incremental theory. The second addend is the corrector term, in fact the plastic contribution to the elastic logarithmic strain rate tensor $\dot{\boldsymbol{E}}_e$, and depends on the plastic deformation gradient $\dot{\boldsymbol{F}}_p$ only, because now the total strain rate external variable $\dot{\boldsymbol{E}}$ is frozen.

2.1 Dissipative terms of the elastic logarithmic strain rate

The stored energy function, or Helmholtz free energy, may be written in terms of any Lagrangian strain measure. The use of logarithmic strain for convenience in this work and the discussed motivation by the rheological model in Fig. 1 lead to an stored energy function written in terms of the total logarithmic and elastic strains as

$$\Psi(\boldsymbol{E}, \boldsymbol{E}_e) = \Psi_{kin}(\boldsymbol{E}) + \Psi_{int}(\boldsymbol{E}_e) \tag{4}$$

DOI: 10.13009/EUCASS2019-1026

where $\Psi_{kin}(\boldsymbol{E})$ is the strain energy function associated to the external variable total strain which operates in the "*external*" spring element, and $\Psi_{int}(\boldsymbol{E}_e)$ is the energy function associated to the internal variable elastic strain which operates within the "*internal*" spring element. The total stored energy Ψ can be split into a volumetric hyperelastic part and a deviatoric elastoplastic part. The stored energy contributions are quadratic in terms of the respective arguments, i.e.

$$\Psi(\boldsymbol{E}, \boldsymbol{E}_e) = \underbrace{\frac{1}{2}\kappa(tr\boldsymbol{E}^v)^2 + \mu_{kin}\boldsymbol{E}^d : \boldsymbol{E}^d}_{\Psi_{kin}} + \underbrace{\mu_{int}\boldsymbol{E}_e^d : \boldsymbol{E}_e^d}_{\Psi_{int}} \tag{5}$$

where μ_{kin} and μ_{int} are the respective elastic material parameters in their deviatoric form: shear moduli (Lame's constant) of the external and internal part, respectively. κ is the bulk modulus. $\boldsymbol{E}^v$ and $\boldsymbol{E}^d$ are the total volumetric and deviatoric logarithmic strain, respectively. $\boldsymbol{E}_e^d$ is the internal deviatoric elastic logarithmic strain. The dissipation rate according to the Clausius-Duhem inequality, may be written as

$$\mathcal{D} = \mathcal{P} - \dot{\Psi} = \mathcal{P} - \dot{\Psi}_{kin} - \dot{\Psi}_{int} \tag{6}$$

where we introduce two important stress tensors (work-conjugate of logarithmic strain measure)

$$\boldsymbol{T}_{kin} = \frac{d\Psi_{kin}(\boldsymbol{E})}{d\boldsymbol{E}} \quad \text{and} \quad \boldsymbol{T}_{int}^{|e} = \frac{d\Psi_{int}(\boldsymbol{E}_e)}{d\boldsymbol{E}_e} = \frac{d\Psi_{int}(\boldsymbol{E}_e)}{d\boldsymbol{E}_e} : \frac{\partial \boldsymbol{E}_e}{\partial \boldsymbol{E}}\bigg|_{\dot{\boldsymbol{F}}_p=\boldsymbol{0}} \tag{7}$$

and the total stress tensor

$$\boldsymbol{T} = \boldsymbol{T}_{kin} + \boldsymbol{T}_{int}^{|e} : \frac{\partial \boldsymbol{E}_e}{\partial \boldsymbol{E}}\bigg|_{\dot{\boldsymbol{F}}_p=\boldsymbol{0}} = \boldsymbol{T}_{kin} + \boldsymbol{T}_{int} \tag{8}$$

and where the stress tensor $\boldsymbol{T}_{kin}$ lies in the reference configuration, as $\boldsymbol{E}$ does, and $\boldsymbol{T}_{int}^{|e}$ lies in the intermediate configuration as $\boldsymbol{E}_e$. The stress tensor $\boldsymbol{T}$ is work-conjugate of the logarithmic strain, and is named in this work as generalized Kirchhoff stress tensor. Both stress tensors in Eq. 7 are not in the same large strain configuration, because $\boldsymbol{T}_{int}^{|e}$ is placed in the intermediate configuration by the elastic predictor, when the plastic corrector starts in the incremental theory. In the infinitesimal description, both tensors are placed in the same and only single configuration. On the other hand, the tensor $\boldsymbol{T}_{kin}$ is an external variable in this model, probably similar to the backstress variable common in other kinematic hardening models, but where this backstress is internal depending on the plastic strain variable, while $\boldsymbol{T}_{kin}$ depends on the total strain.

Considering now Eq. 6 in the case of the elastic strain rate with a frozen total strain rate, so that the nonnull plastic term ($\dot{\boldsymbol{F}}_p \neq \boldsymbol{0}$) motivated by the rheological device shown in Fig. 1, where only the internal branch is dissipative, may be reduced to the expression

$$\mathcal{D} \equiv -\dot{\Psi}_{int}\big|_{\dot{\boldsymbol{E}}=\boldsymbol{0}} = -\boldsymbol{T}_{int}^{|e} : {}^{ct}\dot{\boldsymbol{E}}_e > 0 \quad \text{if} \quad \dot{\boldsymbol{F}}_p \neq \boldsymbol{0} \tag{9}$$

where dissipation is written in terms of symmetric tensors, both of purely elastic nature living in the intermediate configuration. The term ${}^{ct}\dot{\boldsymbol{E}}_e$ is named as the corrector contribution to the elastic logarithmic strain rate $\dot{\boldsymbol{E}}_e$, which it is the power-conjugate of the stress tensor $\boldsymbol{T}_{int}^{|e} = d\Psi_{int}/d\boldsymbol{E}_e$. Note that the frequently used non-symmetric Mandel stress tensor as work-conjugate of the non symmetric plastic velocity gradient tensor, both commonly present in other dissipation equations of the literature, are not present in this model.

This novelty, where the dissipative evolution may be written with the term of elastic strain rate $\dot{\boldsymbol{E}}_e$ in this work, avoids the use of plastic rates and permits us write the associative flow rule as follows

$${}^{ct}\dot{\boldsymbol{E}}_e = -\dot{\gamma}\frac{1}{\frac{2}{3}k}\nabla\phi_T = -\dot{\gamma}\frac{1}{\frac{2}{3}k}\mathbb{N}_T : \boldsymbol{T}_{int}^{|e} \tag{10}$$

where $\mathbb{N}_T$ is the Hill fourth order tensor, that contains the anisotropic plastic material parameters in a fully symmetric form, and where we introduce the use of the anisotropic yield function. In this manner, Eq. 10 provides an orthotropic symmetry to the plastic evolution in the anisotropic behaviour. The term γ is the plastic multiplier or the accumulated plastic strain in the algorithmic solution, and k is the material yield stress parameter. ϕ_T is the plastic potential for Kirchhoff stresses. In the associative form it is equal to the yield function and drives the corrector step to ensure that the stress is always into the elastic domain, to complete the return mapping scheme. From Eq. 9 we can identify the yield function of the elastic generalized Kirchhoff stress tensor when plastic loading condition is fulfilled, written with the stress tensor lying in the intermediate configuration

$$f_T(\boldsymbol{T}_{int}^{|e}, k) = \boldsymbol{T}_{int}^{|e} : \mathbb{N}_T : \boldsymbol{T}_{int}^{|e} - \tfrac{2}{3}k^2 = 0 \quad \text{if} \quad \dot{\gamma} > 0 \tag{11}$$

A very important property of Eq. 10 is that it preserves the classical return mapping schemes of the infinitesimal theory, even in the case of a general orthotropic elastoplastic material. Another key aspect gaining importance is the now possible integration of the dissipative corrector contribution of Eq. 10 in an fully additive manner for large strains as it is done in the infinitesimal theory, thanks to the use of the logarithmic strains in the computational framework.

DOI: 10.13009/EUCASS2019-1026

2.2 Stress integration algorithm

The stress integration algorithm is carried out over Eq. 10, the *elastic* logarithmic strain rate tensor, using a backward-Euler algorithm in the consistent nonlinear equation

$$ {}^{t+\Delta t}_{0}\boldsymbol{E}_e = {}^{t}_{0}\boldsymbol{E}_e + \int_t^{t+\Delta t} {}^{tr}\dot{\boldsymbol{E}}_e d\tau + \int_t^{t+\Delta t} {}^{ct}\dot{\boldsymbol{E}}_e d\tau = {}^{tr}\boldsymbol{E}_e - \frac{\Delta\gamma}{\frac{2}{3}\,{}^{t+\Delta t}k}\mathbb{N}_T : {}^{t+\Delta t}\boldsymbol{T}^{|e}_{int} \tag{12} $$

then written as a residual equation

$$ {}^{t+\Delta t}\rho_e = {}^{t+\Delta t}_{0}\mathbf{E}_e + \frac{\Delta\gamma}{\frac{2}{3}\,{}^{t+\Delta t}k}\,{}^{t+\Delta t}\nabla\phi_T - {}^{tr}\mathbf{E}_e \longrightarrow \mathbf{0} \tag{13} $$

Note that Eq. 12 is a formula valid for large strains but it is also of an additive nature as the small strain case, thanks to the properties of logarithmic strains. This integration algorithm avoids the use of the exponential mapping and ensures an isochoric plastic flow for the pressure-insensitive yield criteria.

Additionally, the rate of the yield function must fulfill the consistency requirement of the Kuhn-Tucker conditions $\dot{f}_T = 0$ when $\dot{\gamma} > 0$ at any time t

$$ \dot{f}_T = \dot{f}_T|_{\boldsymbol{F}_p=\mathbf{0}} + \dot{f}_T|_{\boldsymbol{E}=\mathbf{0}} \tag{14} $$

Both conditions, Eq. 13 and Eq. 2, make up a set of nonlinear equations that must be solved interatively using an Newton-Raphson-type algorithm, with a residual equation ${}^{t+\Delta t}\mathsf{R}^{(j)} \longrightarrow \mathsf{O}$, where (j) represent the local iteration counter for the computational step from the initial algorithmic time t to the final time $t + \Delta t$

$$ {}^{t+\Delta t}\mathsf{R}^{(j)}\left({}^{t+\Delta t}_{0}\mathsf{E}^{(j)}\right) := \left\{ \begin{array}{c} {}^{t+\Delta t}\rho_e^{(j)} \\ {}^{t+\Delta t}f_T^{(j)} \end{array} \right\} \longrightarrow \mathbf{0} \quad \text{with} \quad {}^{t+\Delta t}_{0}\mathsf{E}^{(j)} := \left\{ \begin{array}{c} {}^{t+\Delta t}_{0}\mathbf{E}_e^{(j)} \\ {}^{t+\Delta t}_{0}\gamma^{(j)} \end{array} \right\} \tag{15} $$

where the tangent matrix is obtained as

$$ \nabla^{t+\Delta t}\mathsf{R} = \left[\begin{array}{cc} \dfrac{d^{t+\Delta t}\boldsymbol{\rho}_{int}}{d\,{}^{t+\Delta t}_{0}\boldsymbol{E}_e} & \dfrac{d^{t+\Delta t}\boldsymbol{\rho}_{int}}{d\Delta\gamma} \\ \dfrac{d^{t+\Delta t}f_T}{d\,{}^{t+\Delta t}_{0}\boldsymbol{E}_e} & \dfrac{d^{t+\Delta t}f_T}{d\Delta\gamma} \end{array} \right] \tag{16} $$

Once the solution has converged in the local Newton-Raphson algorithm, ${}^{t+\Delta t}\boldsymbol{E}_e$ and ${}^{t+\Delta t}\gamma$ are directly obtained. Afterwards, internal stresses ${}^{t+\Delta t}\mathbf{T}^{|e}_{int}$ are calculated in the updated intermediate configuration.

The next step is to obtain the elastoplastic tangent modulus of the rheological device, which adopts exactly the same form as it does in the infinitesimal strains case.

2.3 Computational algorithmic scheme

Finite element programs work commonly with a total Lagrangian formulation for large displacements and strains, and use the second Piola-Kirchhoff stress tensor as work-conjugate of the Green-Lagrange strain tensor. Our model works with logarithmic strains and generalized Kirchhoff stress and this forces us to translate the internal variables in order to measure the stress tensor variable used by finite elements, in this case through the consistent algorithmic operation

$$ {}^{t+\Delta t}\mathbf{S}_{int} = {}^{t}_{0}\mathbf{X}_p^{-1}\left({}^{t+\Delta t}\mathbf{T}^{|tr}_{int} : \frac{d\,{}^{tr}\mathbf{E}_e}{d\,{}^{tr}\mathbf{A}_e}\right){}^{t}_{0}\mathbf{X}_p^{-T} \tag{17} $$

$$ {}^{t+\Delta t}\boldsymbol{S} = {}^{t+\Delta t}\boldsymbol{S}_{kin} + {}^{t+\Delta t}\boldsymbol{S}_{int} \tag{18} $$

finally we obtain the second Piola-Kirchhoff stress tensor ${}^{t+\Delta t}\boldsymbol{S}$ in each Gaussian integration point, updated and mapped into the reference configuration. This term is necessary to update the geometrical stiffness matrix in the nonlinear finite element code, as indicated in Fig. 2. The term $(d\,{}^{tr}\mathbf{E}_e/d\,{}^{tr}\mathbf{A}_e)$ is the fourth order mapping tensor from logarithmic strains to Green-Lagrange quadratic strains, both in the intermediate configuration.

The second necessary term to complete the integration algorithm is the elastoplastic tangent modulus, obtained through the proper mapping operation performed in Eq. 17, but mathematically more complex, of which details are out of the scope of this paper. As usually done in Total Lagrangian finite element codes, we obtain the elastoplastic modulus through the algorithmic consistent operation carried out as

DOI: 10.13009/EUCASS2019-1026

$$ {}^{t+\Delta t}\mathbb{C}_{ep} = \frac{d\,{}^{t+\Delta t}\mathbf{S}_{int}}{d\,{}^{t+\Delta t}{}_{0}\mathbf{A}} \tag{19} $$

The developed numerical algorithm for contribution to stresses is summarized in Box 1 (2.3). This scheme has been implemented into a user material subroutine in ADINA® commercial program [3] via UCMAT3 user subroutine in *.dll* format for applications to sheet metal forming, and in this paper applied to simulate the springback problem inherent to sheet metal forming.

ADINA® provides an implicit integration scheme for global solution of the finite element model, using by default the Newton-Raphson method, but applied to the problem over the finite element nodal variables, and with a Total Lagrangian formulation for large displacement/strain formulation. Therefore, we need to return the second Piola-Kirchhoff stress tensor $\boldsymbol{S}$ and its related consistent tangent modulus $\mathbb{C}$ to the main program, as it is schematized in Fig. 2.

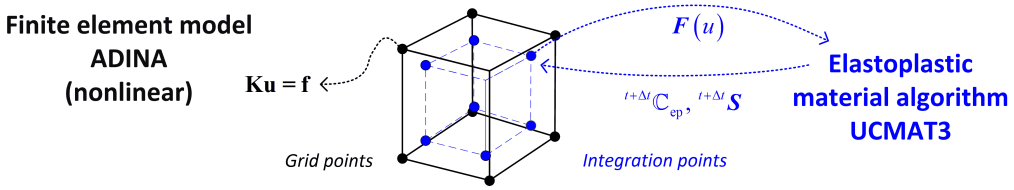

Figure 2: Computational scheme between ADINA® program and our user elastoplastic material subroutine, in terms of consistent algorithmic variables.

3. Application for Sheet Metal Forming: Springback Prediction

In the automotive and aeronautic industry, new sheet metal parts are designed using finite element method software. Industrial requirements such as fits and clearances or surface roughness are not well satisfied by today's accuracy of these simulations. One of these limitations is the accurate prediction of springback and that is why the phenomenon of springback and its analysis are growing concern in sheet metal forming industry. Under these circumstances this paper deals with this analysis in order to validate the material model addressed in the previous sections.

Table 1: Nomenclature for material parameters.

E	Elastic Modulus (N/mm^2)
ν	Poisson's Ratio (-)
k_0	Reference Yield Stress (N/mm^2)
k_∞	Limit Stress Parameter (N/mm^2)
H	Real Linear Hardening Modulus (N/mm^2)
β	Mixed Hardening Parameter [a] (-)
$\bar{H}$	Effective [b] Linear Hardening Modulus (N/mm^2)
δ	Voce Hardening Parameter (-)
a, b, c, f, g, h	Hill's anisotropy parameters [c] (-)
$2\mu_{int}$	Internal Shear Moduli (N/mm^2)
$2\mu_{kin}$	External/Kinematic Shear Moduli (N/mm^2)

[a] $\beta = 1$ for isotropic hardening, $\beta = 0$ for kinematic hardening
[b] $\bar{H} = \beta H$. See [2]
[c] Hill's anisotropy parameters have been standarized (See [4])

3.1 Calibration of Elasto-plastic Parameters

In this paper, we study different materials (DP600 dual phase steel and AA6111-T4 aluminium) and hardening configurations. In [6] it is shown that to fit the elasto-plastic hardening parameters, the uniaxial tensile test is not enough to reproduce and identify a valid combination of material parameters for a combined hardening model and cyclic experiments must be performed. The lack of experimental data and the difficult attainment of these tests (specially the in-plane compression phase) leads to obtain these parameters by the uniaxial tensile experimental data and a subsequent

DOI: 10.13009/EUCASS2019-1026

Box 1: Implicit stress integration algorithm.

1. Trial elastic predictor; geometric preprocessor: given ${}^{t+\Delta t}_{0}\boldsymbol{F}$, ${}^{t}_{0}\boldsymbol{F}_p$ and ${}^{t}_{0}\gamma$, compute the trial elastic predictor state

$$
\begin{aligned}
{}^{tr}\boldsymbol{F}_p &:= {}^{t}_{0}\boldsymbol{F}_p; \quad {}^{tr}\boldsymbol{F}_e := {}^{t+\Delta t}_{0}\boldsymbol{F}\,{}^{t}_{0}\boldsymbol{F}_p \\
{}^{tr}\boldsymbol{E}_e &:= \frac{1}{2}\ln({}^{tr}\boldsymbol{F}_e^{T\,tr}\boldsymbol{F}_e); \quad {}^{tr}\boldsymbol{T}^{|e}_{int} := \frac{d\Psi_{int}({}^{tr}\boldsymbol{E}_e)}{d^{tr}\boldsymbol{E}_e}
\end{aligned}
$$

2. Check yield condition and test for plastic loading

$$
\begin{aligned}
&{}^{tr}k := {}^{t}k \\
&{}^{tr}f_T := f_T({}^{tr}\boldsymbol{T}^{|e}_{int}, {}^{tr}k) = {}^{tr}\boldsymbol{T}^{|e}_{int} : \mathbb{N}_T : {}^{tr}\boldsymbol{T}^{|e}_{int} - \tfrac{2}{3}{}^{tr}k^2 \\
&\text{IF} \quad {}^{tr}f_T \le 0 \quad \text{THEN} \\
&\quad \textit{Elastic step:} \ \text{set} \quad {}^{t+\Delta t}(\bullet) = {}^{tr}(\bullet) \\
&\text{ELSE} \\
&\quad \textit{Plastic step:} \ \text{Proceed to step 3} \\
&\text{ENDIF}
\end{aligned}
$$

3. Return mapping

   (a) Local Newton iterations: elastic corrector
   Solve iteratively $\mathsf{R}({}^{t+\Delta t}\boldsymbol{E}_e, \Delta\gamma) = \begin{Bmatrix} {}^{t+\Delta t}\boldsymbol{\rho} \\ {}^{t+\Delta t}f_T \end{Bmatrix} = \boldsymbol{0}$ using the Newton-Raphson method with initial values for first iteration ${}^{t+\Delta t}\boldsymbol{E}_e^{(0)} = {}^{tr}\boldsymbol{E}_e$, $\Delta\gamma^{(0)} = 0$ and ${}^{t+\Delta t}k^{(0)} = k({}^{t}\gamma)$

   (b) Update the state variables

$$
{}^{t+\Delta t}\boldsymbol{T}^{|tr}_{int} \simeq {}^{t+\Delta t}\boldsymbol{T}^{|e}_{int} = \left.\frac{d\Psi_{int}(\boldsymbol{E}_e)}{d\boldsymbol{E}_e}\right|_{t+\Delta t}
$$

   Perform mappings to stress/strain quantities, e.f compute the consistent elastoplastic tangent modulus during this phase.

   (c) Compute consistent tangent and update plastic deformation gradient ${}^{t+\Delta t}_{0}\boldsymbol{F}_p$

4. Perform mappings to the stress and strain quantities, e.g. ${}^{t+\Delta t}\boldsymbol{S}$ and ${}^{t+\Delta t}_{0}\boldsymbol{A}$ in the case of Total Lagrangian formulations.

5. EXIT

validation in a finite element method framework. This said, the fit of the hardening model parameters is achieved by the use of the least-squares method. Table 1 contains the followed nomenclature in this work and Table 2 summarizes the set of parameters for each analysed material. Parameters are curve-fitted into a Voce-type isotropic hardening law:

$$
k = k_0 + \bar{H}\gamma + (k_\infty - k_0)(1 - e^{-\delta\gamma}) \tag{20}
$$

Material #146 (AA6111-T4) has been calibrated following a Swift-Nadai hardening law as shown in Fig. 3. In Materials #115, #118 and #122 (DP600), curves has been fitted into experimental data points (Fig. 4). The part of the curves represented is the tensile plastic range of the material model. Note that only a combined hardening approach results in a successful curve fit. One of the main reasons is the 'so-called' Bauschinger effect which causes a reduction of the yield stress upon reverse loading after plastic deformation as presented in [8]. As stated in [5, 8], the single use of an isotropic hardening law results in an unreliable prediction of springback. In Section 3.2.2, this will be a matter of discussion. Fig. 5 shows the r-value anisotropy predicted by our model in application to Material #146.

DOI: 10.13009/EUCASS2019-1026

Table 2: Material Parameters.

Material	**#146**	**#115**	**#118**	**#122**
E	70 500	192 875	192 875	192 875
ν	0.34	0.33	0.33	0.33
k_0	181.24	325	321.23	322.64
k_∞	248.28	726	-	624.10
$\bar{H}$	782.94	104.21	0	- 351.27
δ	50.836	20.083 [a]	0	27.594
b/a	1.4371	1	1	1
c/a	1.5679	1	1	1
f/a	0.9207	1	1	1
g/a	1.0000	1	1	1
h/a	1.0000	1	1	1
$2\mu_{int}$	52 611.94	145 018.80	143 335.20	143 966.13
$2\mu_{kin}$	0	0	1 683.6	1 052.7

[a] This parameter value matches extremely well with the equivalent one presented in [5].

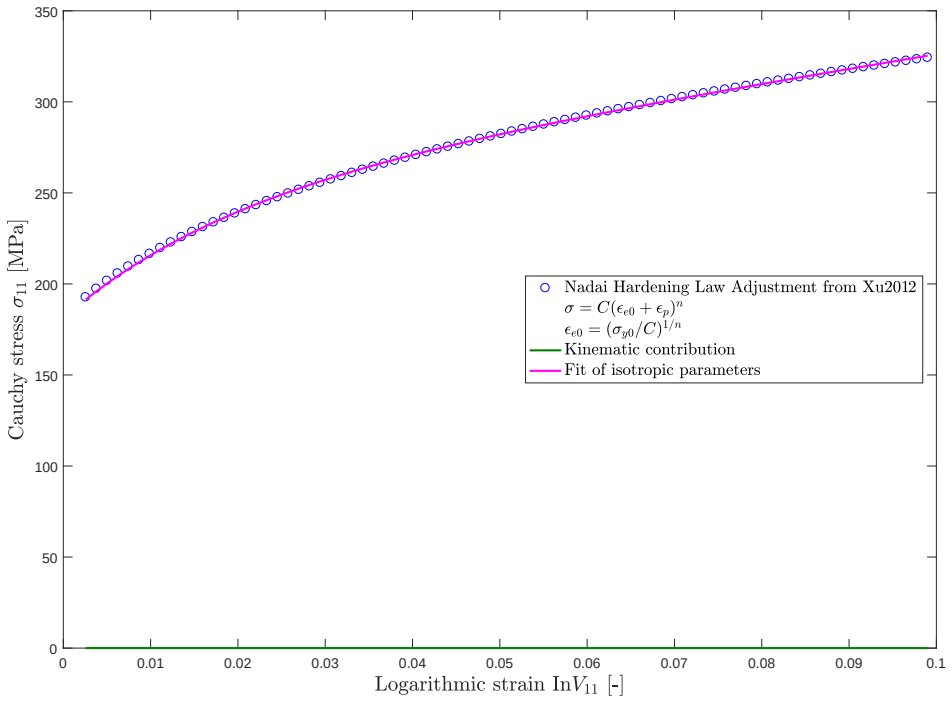

Figure 3: Calibration of Material #146. Nadai Hardening Law Adjustment from [7] and fit of isotropic parameters.

3.2 FEM Modeling and Simulation Results

Simulation will be carried out in the commercial software ADINA®. Both simulation benchmarks presented are static implicit analyses. Modeling techniques may be found by the reader in [3].

3.2.1 Unconstrained Cylindrical Bending Test

The Unconstrained Cylindrical Bending Test is one of the problems addressed as a benchmark at the 5^{th} International Conference and Workshop on Numerical Simulation of 3D Sheet Forming Processes (Numisheet 2002). Even though its importance is relative when it comes to industrial application, its severe springback problems lead to a perfect and

DOI: 10.13009/EUCASS2019-1026

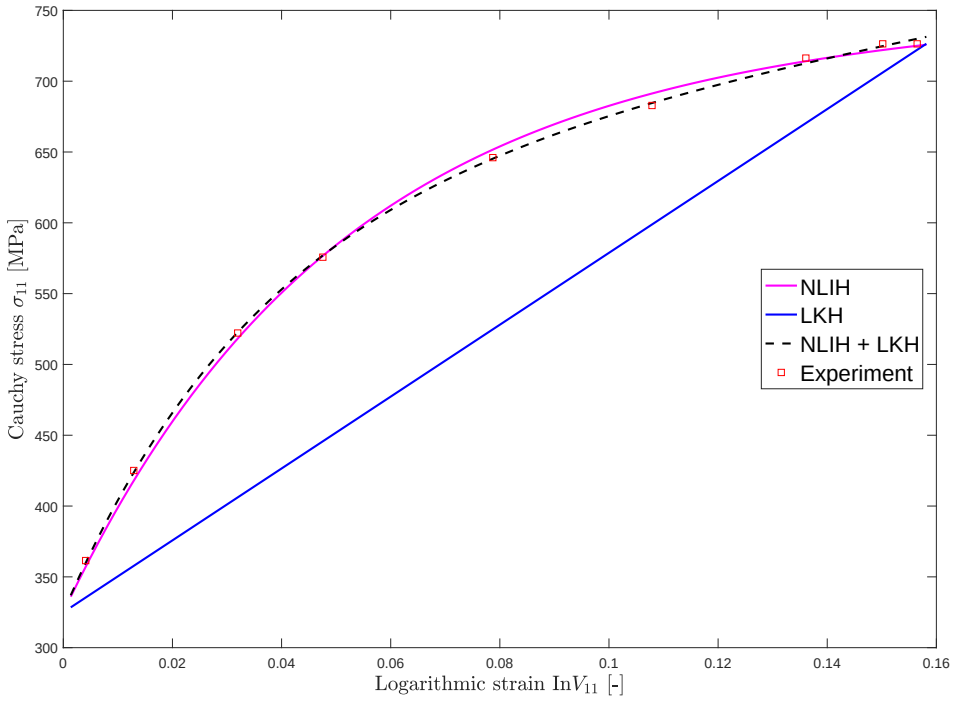

Figure 4: Calibration of Material #115 (NLIH; Nonlinear Isotropic Hardening), Material #118 (LKH; Linear Kinematic Hardening) and Material #122 (NLIH + LKH; Combined Hardening).

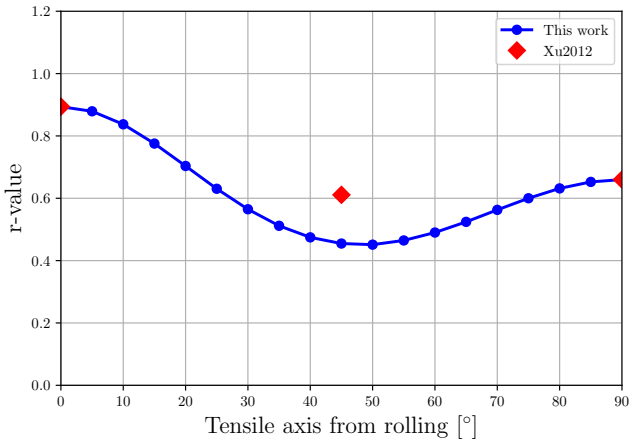

Figure 5: Evolution of the coefficient of anisotropy (r-value) in the plane of the sheet metal for Material #146. Comparison with Xu2012 [7].

sensitive environment of structural analysis [9]. That is the reason experimental results are quite dissimilar to others (under the same laboratory conditions). This is also comparably to numerical testing. Experimental results have been obtained from [10].

The experimental set-up is shown in Fig. 6. The dimensions of the model parameters are presented in Table 3. Assuming that the punch is initially in contact with the sheet, the bending process spans the whole punch stroke. This leads to a final concentric layout of the cylindrical surfaces (R1 and R2). Note that a clearance of 0.5mm per radial contact is left behind. As proposed in Numisheet 2002 [10], the punch and the die are assumed as rigid contact surfaces. 3D Contact (μ = 0.1348) is assumed between the hardened tools and the sheet. An interested reader may find

DOI: 10.13009/EUCASS2019-1026

useful [3] for a proper and accurate adjustment of the contact and friction parameters. Symmetry has not been taken into account in order to not intercede in the unconstrained approach of the analysis. Meinders et al. in [9] demonstrated that the punch velocity has just a minor effect on the springback angle results. Anyhow, the punch speed has been set to 500 mm/s as proposed in [7]. The initial blank (120 mm x 30 mm x 1 mm) is meshed with our 8-node Q1/P0 brick mixed u/p finite elements (270 x 10 x 1). The rest of the meshes are presented in Fig. 7.

Fig. 8 shows the deformed shape of the metal sheet at punch stroke = 14 mm and the definition of the angle between OI and OJ (ψ). Points I and J are used to mark the critical points of the punch (target surface). The critical points are the last nodes to get in contact with the blank upper surface (contactor surface). Point O is the centre of the cylindrical punch. In Table 4 a correlation between time (t), punch stroke (PS) and angle (ψ) is presented. Note that the punch stroke is a function of time and the already defined punch velocity. In Fig. 13 a comparison between this work, experimental data and [7] is given. This example proves that our material model applied to 8-node Q1/P0 brick mixed u/p finite elements performs the contact problem extremely well and provides a very precise calculation of the forming angle throughout the whole bending process.

The angle used to measure the forming and after-springback deformed blank geometry is shown in Fig. 14. Springback phase is simulated by the use of contact death and tooling removal. Figs. 9, 10, 11 and 12 show the effective stress of the deformed specimen during the bending phase and after springback is completely finished. Table 5 includes the experimental and simulations results of [7] solid-shell and this work's simulation results. The results confirm a better prediction of the forming angle (θ_1) over the springback angle (θ_2) in line with the benchmark results analysis presented in [9] and [10]. Fig. 15 shows the typical global convergence rates of the algorithm for this simulation. To improve the nonlinear analysis convergence of this model, the line search algorithm provided by ADINA® has been implemented into the model.

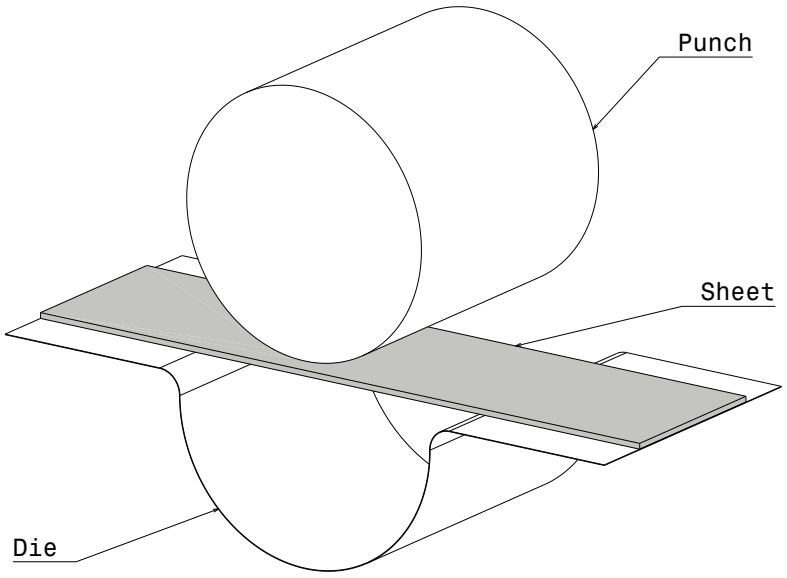

Figure 6: Isometric view of the tooling geometry layout of the unconstrained cylindrical bending test.

Table 3: Evolution of ψ as a function of the punch stroke and corresponding time.

Model Parameter	(mm)	**Model Parameter**	(mm)
Punch radius (R1)	23.5	Sheet thickness	1.0
Die radius (R2)	25.0	Punch width	50.0
Die shoulder radius (R3)	4.0	Punch stroke	28.5 [a]
Die width	50.0	Sheet width	30.0

[a] Punch stroke = 27.5mm + blank thickness

DOI: 10.13009/EUCASS2019-1026

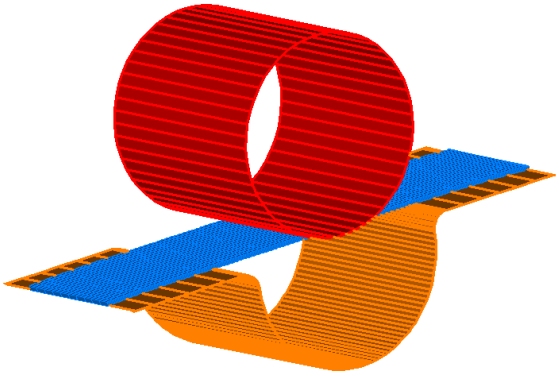

Figure 7: FE model for unconstrained bending problem.

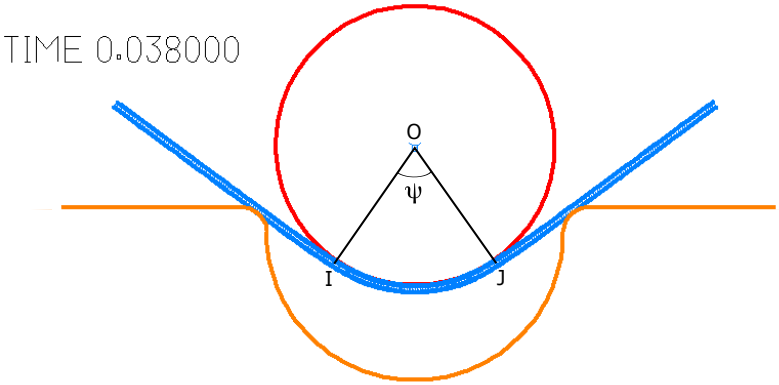

Figure 8: Deformed shape at PS = 14 mm. Definition of angle ψ.

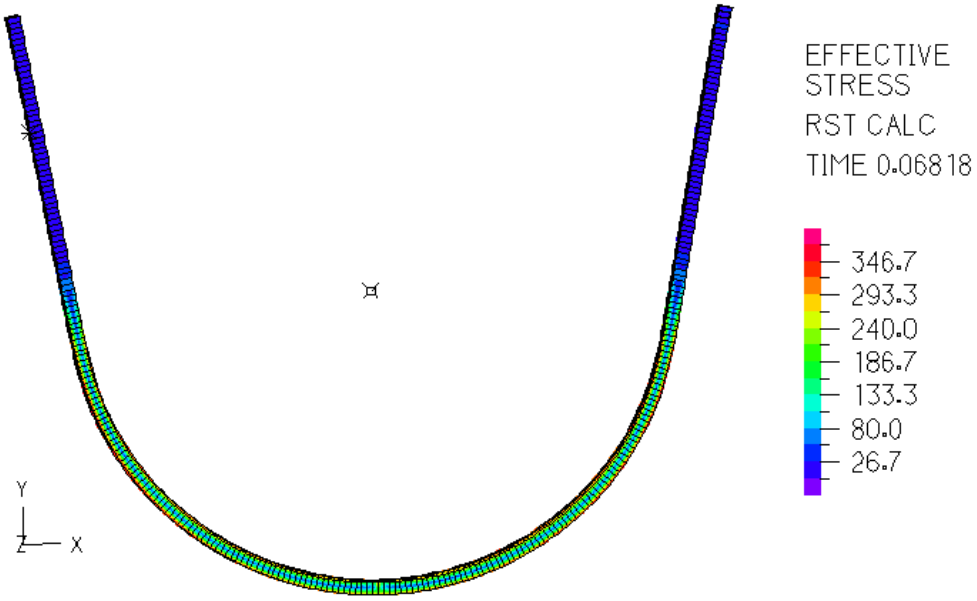

Figure 9: Effective stress at the end of the forming phase. Front view.

DOI: 10.13009/EUCASS2019-1026

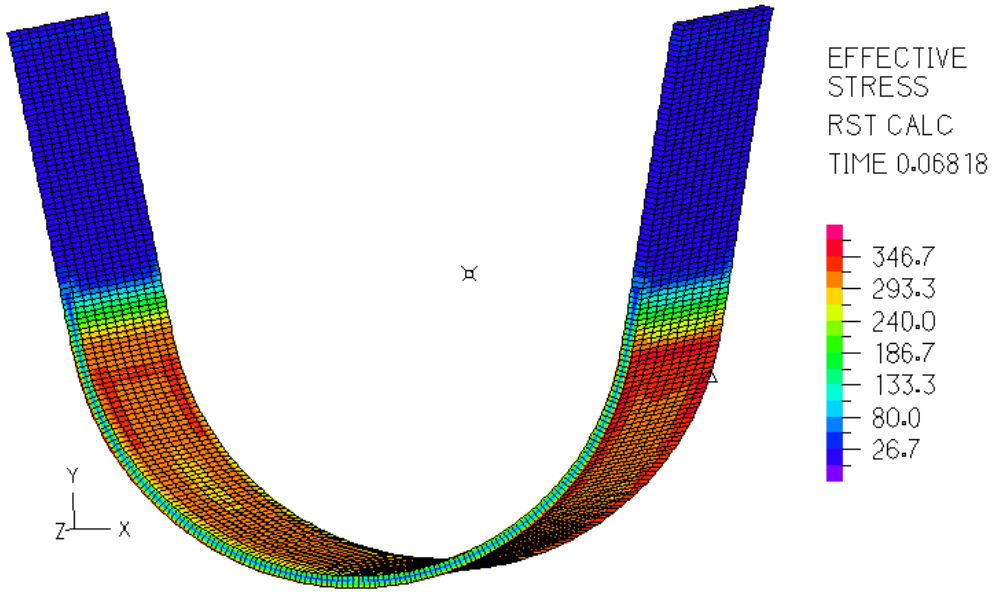

Figure 10: Effective stress at the end of the forming phase. Perspective view.

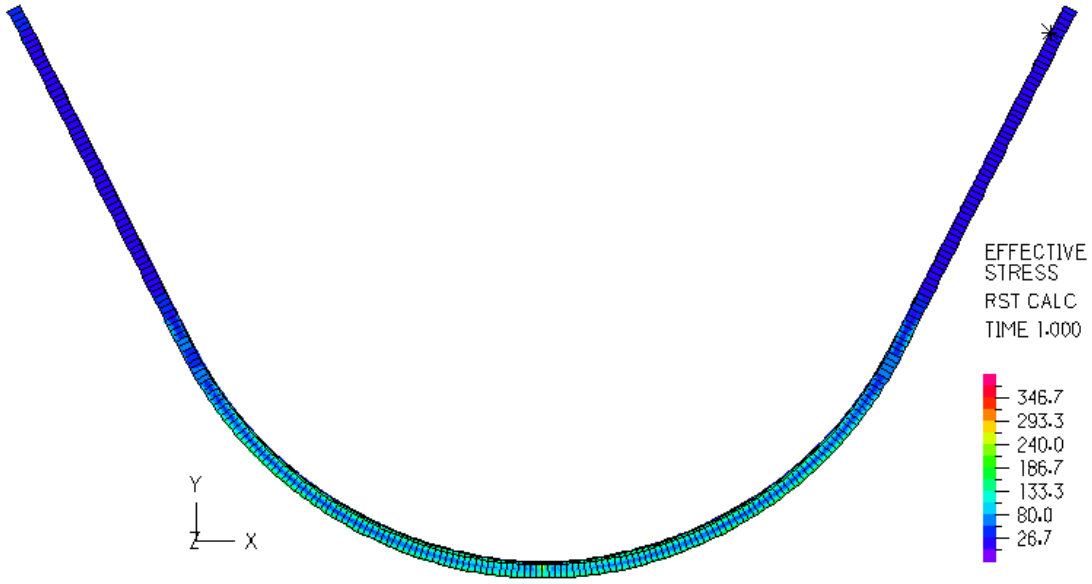

Figure 11: Effective stress after springback. Front view.

Table 4: Correlation between time, punch stroke and angle.

Angle [°]	Punch Stroke [mm]	Time [a] [s]
$\psi_1 = 17.65$	$PS_1 = 7$	$t_1 = 0.024$ [b]
$\psi_2 = 60.00$	$PS_2 = 14$	$t_2 = 0.038$
$\psi_3 = 116.47$	$PS_3 = 21$	$t_3 = 0.052$
$\psi_4 = 158.82$	$PS_4 = 28.5$	$t_4 = 0.067$

[a] Punch speed = 500 mm/s

[b] Effective contact starts at t* = 0.015

3.2.2 Draw-Bending Test

This second simulation example reproduces the process of "bending under tension" or draw-bending test. Its analysis consists in the prediction of springback in a narrow sheet metal strip and its impact is considerably substantial as it

DOI: 10.13009/EUCASS2019-1026

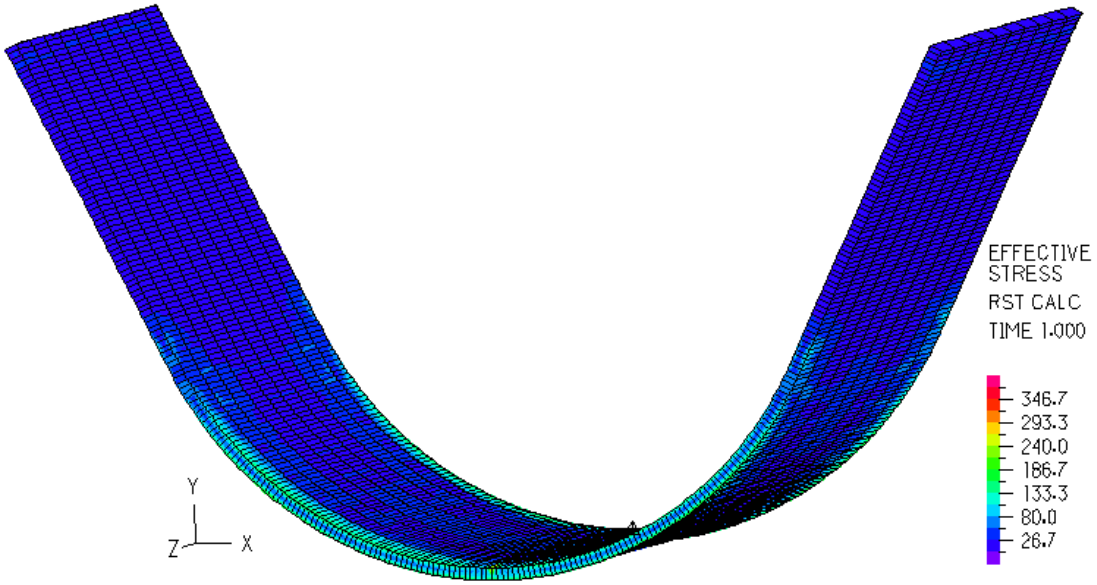

Figure 12: Effective stress after springback. Perspective view.

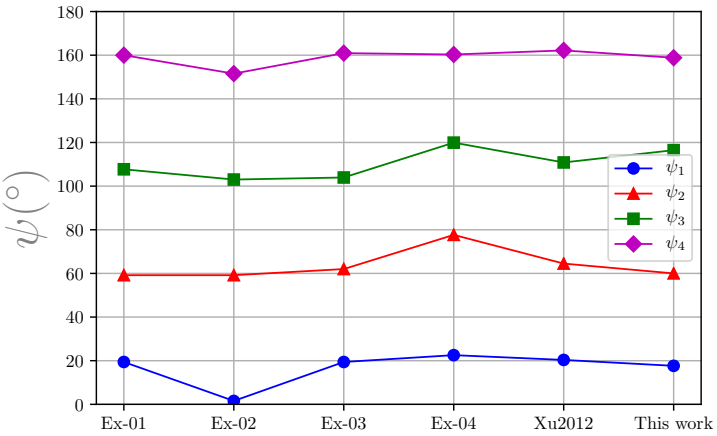

Figure 13: Comparison of the angles between OI and OJ (ψ_i).

Table 5: Comparison of the angles before and after springback.

	$\theta_1[^\circ]$: Forming angle	$\theta_2[^\circ]$ Springback angle
Ex-01	20.5	56.5
Ex-02	21.1	56.1
Ex-03	20.3	58.1
Ex-04	20.6	57.2
Xu2012 [7]	21.2	59.1
This work	20.9	54.1

presents similarities with industrial sheet forming operations. In this process, the strip is subjected to a pre-bending phase, a posterior bending phase and a last removal phase from the tooling. The machine involved in the experiments consist of two clamps jaws in which the flat strip is located as addressed in [5, 6]. These jaws are positioned in a perpendicular way to each other in order to let the strip bend over a roller. The roller, which may be fixed or rotating, is simulated by a rigid cylindrical surface. The contact between the strip and the roller is presented as a 3D Contact problem with a friction coefficient of $\mu = 0.02$ as the roller is considered to be a rotating bending tool. Fig. 16 shows the experimental layout of the test. While the left clamping zone is controlled by terms of displacement, the right one

DOI: 10.13009/EUCASS2019-1026

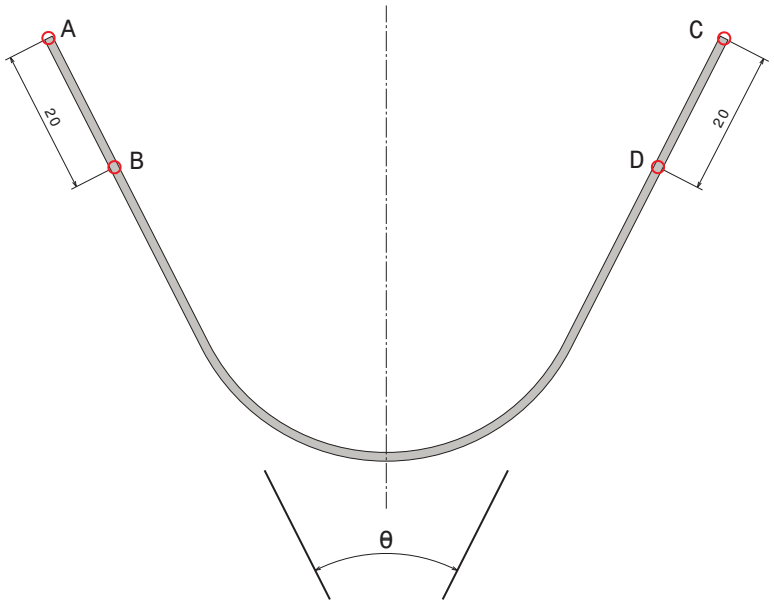

Figure 14: Definition of the angle to measure forming and after-springback geometry.

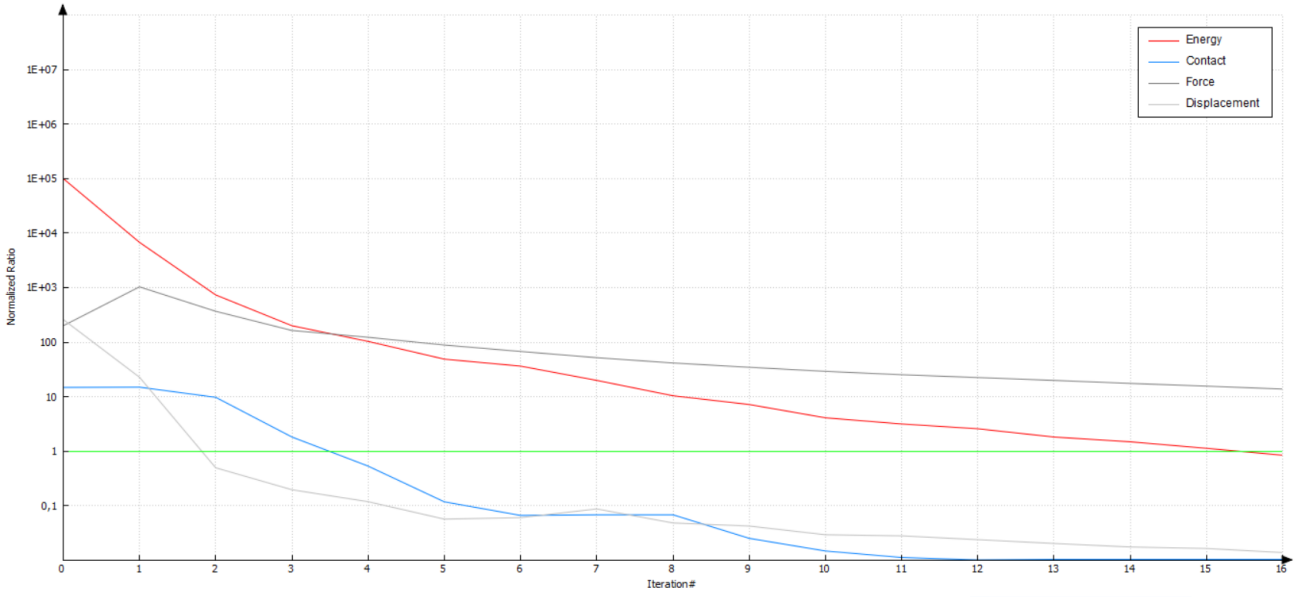

Figure 15: Typical global convergence rates obtained from ADINA® at the initial stage of the unconstrained bending process.

is subjected to a tensile force. As suggested in [6] the tensile force has been set to $F = \alpha A \sigma_{y0}$, where F is the tensile force, A is the sheet metal section area, σ_{y0} is the initial yield stress and α is a correction factor ($\alpha = 0.5$). After being drawn up to a prescribed distance $\Delta x = 95$ mm, the specimen is unloaded and removed from the tooling in order to let it spring-back. The strip is initially a 356 mm x 50 mm x 1 mm blank meshed with our 8-node Q1/P0 brick mixed u/p finite elements (170 x 5 x 1). Elseways, the geometric parameters of the roller are $R = 5$ mm and $L = 60$ mm. An isometric view of the meshes at the start of the pre-bending process is shown in Fig. 17.

As it can be seen in Fig. 18, using only an isotropic hardening law (Material#115) leads to an overprediction of the springback in the specimen while the alone use of kinematic hardening (Material#118) leads to an underprediction of the studied phenomenon. Therefore, it is necessary to use a combined hardening approach (Material #122) in order to obtain a successful prediction of the springback geometry (the most fitted case in the plastic zone of the strip profile). Note that the value of the correction factor has a major influence on the right flat zone of the strip profile.

DOI: 10.13009/EUCASS2019-1026

This imbalance could be fixed with the calculation of the correct value of the tensile force in the experiment or the re-calibration of the material model by adjusting the kinematic contribution (adjustment of τ_{yc}; see [1]). In order to keep this paper in some reasonable dimensions, this case study will not be considered. An interested reader may find usefulness in the reading about this correction factor or "normalized back force" in [11].

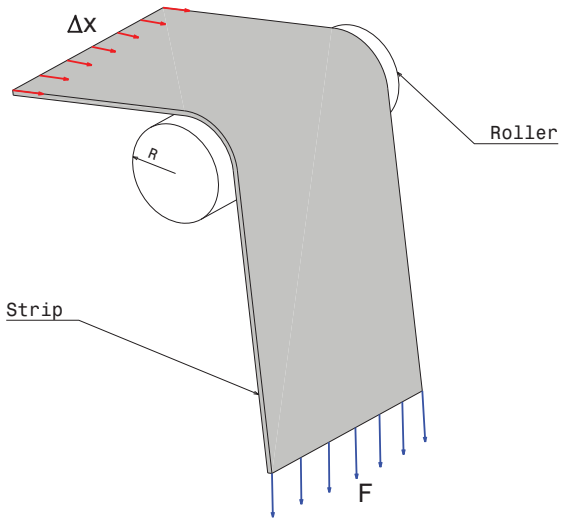

Figure 16: Isometric view of the tooling geometry of the draw-bending test during the drawing phase.

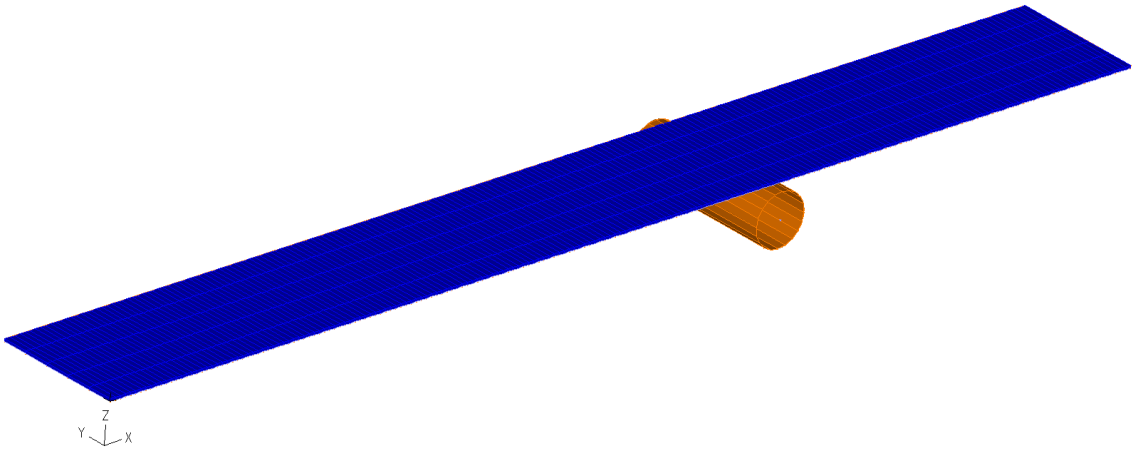

Figure 17: Isometric view of the FE model for the draw-bending test.

4. Acknowledgments

Partial financial support for this work has been given by grant PGC 2018-097257-B-C32 from the Dirección General de Proyectos de Investigación of the Ministerio de Economía y Competitividad of Spain. The ADINA® program license used in this work has been a courtesy of ADINA R&D to the UPM.

References

[1] Miguel Á. Sanz, Francisco J. Montáns, and Marcos Latorre. Computational anisotropic hardening multiplicative elastoplasticity based on the corrector elastic logarithmic strain rate. *Computer Methods in Applied Mechanics and Engineering*, 320:82–121, jun 2017.

DOI: 10.13009/EUCASS2019-1026

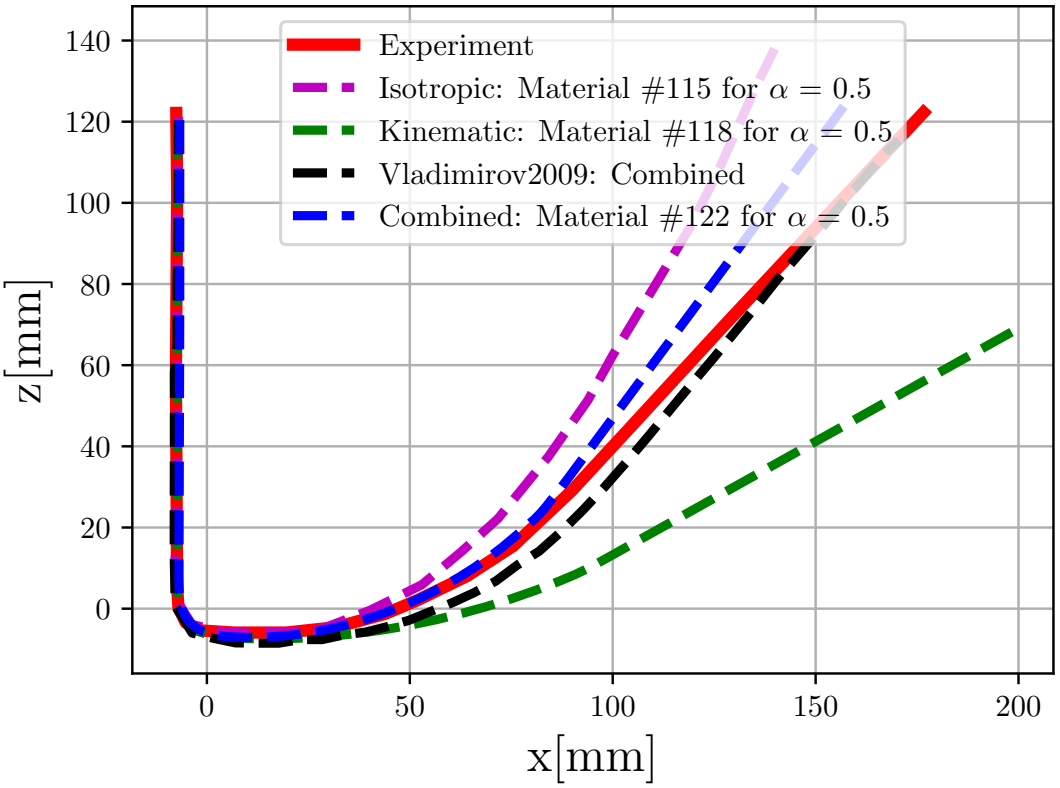

Figure 18: Comparison between experimental, Vladimirov2009 [5] and this work's strip profiles after springback.

[2] Miguel Á. Sanz, K. Nguyen, Marcos Latorre, Manuel Rodríguez, and Francisco J. Montáns. Sheet metal forming analysis using a large strain anisotropic multiplicative plasticity formulation, based on elastic correctors, which preserves the structure of the infinitesimal theory. *Finite Elements in Analysis and Design*, jul 2019.

[3] ADINA R & D. Theory and Modeling Guide. Technical report, ADINA R & D, Inc., Boston, Massachusets, 2012.

[4] Milos Kojic and Klaus-Jürgen. Bathe. *Inelastic analysis of solids and structures*. Springer, 2005.

[5] I.N. Vladimirov, M.P. Pietryga, and S. Reese. Prediction of springback in sheet forming by a new finite strain model with nonlinear kinematic and isotropic hardening. *Journal of Materials Processing Technology*, 209(8):4062–4075, apr 2009.

[6] Marco Schwarze, Ivaylo N. Vladimirov, and Stefanie Reese. Sheet metal forming and springback simulation by means of a new reduced integration solid-shell finite element technology. *Computer Methods in Applied Mechanics and Engineering*, 200(5-8):454–476, jan 2011.

[7] H.J. Xu, Y.Q. Liu, and W. Zhong. Three-dimensional finite element simulation of medium thick plate metal forming and springback. *Finite Elements in Analysis and Design*, 51:49–58, apr 2012.

[8] K. M. Zhao and J. K. Lee. Material Properties of Aluminum Alloy for Accurate Draw-Bend Simulation. *Journal of Engineering Materials and Technology*, 123(3):287, 2001.

[9] T. Meinders, A. W. A. Konter, S. E. Meijers, E. H. Atzema, and H. Kappert. A Sensitivity Analysis On The Springback Behavior Of The Unconstrained Bending Problem. In *AIP Conference Proceedings*, volume 778, pages 272–277. AIP, aug 2005.

[10] D.Y. Yang. *NUMISHEET 2002: Proceedings of the 5th International Conference and Workshop on Numerical Simulation of 3D Shell Forming Processes -verification of Simulation with Experiment-*. 2002.

[11] W.D Carden, L.M Geng, D.K Matlock, and R.H Wagoner. Measurement of springback. *International Journal of Mechanical Sciences*, 44(1):79–101, jan 2002.